Formation of Bi_2Ir Nanoparticles in a Microwave-Assisted Polyol Process Revealing the Suboxide Bi_4Ir_2O

Matthias Smuda,[a] Kati Finzel,[a] Martin Hantusch,[b] Jonas Ströh,[c] Nicole Pienack,[c] Azat Khadiev,[d] Huayna Terraschke,[c] Michael Ruck,[a, e] and Thomas Doert*[a]

[a] M. Smuda, Dr. K. Finzel, Prof. Dr. Th. Doert, Prof. Dr. M. Ruck
Faculty of Chemistry and Food Chemistry
Technische Universität Dresden
01062 Dresden, Germany
E-mail: thomas.doert@tu-dresden.de

[b] Dr. M. Hantusch
Leibniz Institute for Solid State and Materials Research (IFW Dresden)
Helmholtzstr. 20, 01069 Dresden, Germany

[c] J. Ströh, Dr. N. Pienack, Jun.-Prof. Dr. H. Terraschke
Institute of Inorganic Chemistry
Christian-Albrechts-Universität zu Kiel
Max-Eyth-Str. 2, 24118 Kiel, Germany

[d] Dr. A. Khadiev
Deutsches Elektronen-Synchrotron DESY
Notkestr. 85, 22607 Hamburg, Germany

[e] Max Planck Institute for Chemical Physics of Solids
Nöthnizer Str 40, 01187 Dresden, Germany

Abstract

Intermetallic phases are usually obtained by crystallization from the melt. However, phases containing elements with widely different melting and boiling points, as well as nanoparticles, which provide a high specific surface area, are hardly accessible via such a high-temperature process. The polyol process is one option to circumvent these obstacles by using a solution-based approach at moderate temperatures. In this study, the formation of Bi_2Ir nanoparticles in a microwave-assisted polyol process was investigated. Solutions were analyzed using UV-Vis spectroscopy and the reaction was tracked with synchrotron-based *in-situ* powder X-ray diffraction (PXRD). The products were characterized by PXRD and high-resolution transmission electron microscopy. Starting from $Bi(NO_3)_3$ and $Ir(OAc)_3$, the new suboxide Bi_4Ir_2O forms as an intermediate phase at about 160 °C. Its structure was determined by a combination of PXRD and quantum-chemical calculations. Bi_4Ir_2O decomposes in vacuum at about 250 °C and is reduced to Bi_2Ir by hydrogen at 150 °C. At about 240 °C, the polyol process leads to the immediate reduction of the two metal-containing precursors and crystallization of Bi_2Ir nanoparticles.

Introduction

The targeted synthesis of materials often requires knowledge of the formation process. In the case of high-temperature syntheses, elucidation of the reaction mechanism and identification of intermediates are major challenges. This is particularly the case for alloys and intermetallic compounds, which are traditionally synthesized by melting the elements together. Crystallization from a hot melt is a process that can only be controlled to a limited extent. In addition typical obstacles, such as peritectic phase formation or large differences in the melting and boiling points of the starting materials, can lead to chemically inhomogeneous products. Even in the favorable case, where all thermodynamic parameters of the system are known and

controllable, various kinetic effects may result in undesirable by-products. Moreover, the typical product of solidification of a melt is an ingot, and many intermetallic compounds are either too hard or too soft for grinding, making inaccessible fine powders with a high specific surface area and a defined morphology that could be valuable for heterogeneous catalysis, for example.

To circumvent these problems, new synthetic strategies have been developed that provide access to powders of intermetallic compounds at moderate temperatures using reactive precursors. One of these is the polyol process,[1] in which polyalcohols (polyols) serve simultaneously as solvents, capping agents and reducing agents. The polyol molecules act as bidentate ligands and are therefore capable of dissolving metal salt precursors in a manner similar to water.[2] Ideally, these polyols also bind to the surface of the newly formed particles, stabilizing them and preventing agglomeration to some extent. Additionally, some influence on the morphology and size of the particles is gained by the choice of the polyol.[3] The main task of the polyalcohol, however, is the reduction of the metal cations. Since the reducing power of a particular polyol increases with temperature, higher temperatures are required for base metals, such as cobalt or nickel, than for iridium or gold, for example.[4] The boiling point of the polyol, however, is a limiting factor. Although higher polyols with higher boiling points can be used, their reduction power is lower than that of the short-chain ones.[4] One way to expand the useable reduction potential is to use a synthesis microwave, in which the reactions are carried out in a closed vessel, allowing reaction temperatures well above the boiling point of the polyol. The precise control of parameters *in-situ* paired with fast heating rates and homogeneous heat distribution enable good reproducibility and make this setup ideal for the investigation of reaction pathways.

A large variety of different binary and even ternary intermetallic phases were prepared using this setup.[5–8] In most cases, a quantitative yield could be achieved by empirical optimization of the reaction parameters. Still little is known about the details of the reaction mechanisms and the crystallization process. Numerous experimental and theoretical studies have been performed on the mechanism of mono-metallic nanoparticles[9–15], but only a few systematic studies allowed to establish a set of principles for the synthesis of intermetallic particles by the (microwave assisted) polyol process.[16–20] Parameters that have a profound impact on the synthesis are, for example, the temperature, the concentrations and the molar ratio, the solvent, the pH value, the accompanying anions, and additional surfactants.[21–23] However, the mechanism cannot be generalized, but strongly depends on the combination of metals. As had been shown, the formation of crystalline BiNi powders starts with the successive reduction of bismuth(III) and nickel(II) cations, leading to bimetallic core-shell nanoparticles "Bi@Ni". Successive diffusion of nickel into the inner bismuth core leads to the intermediate formation of the bismuth-rich compound Bi_3Ni, which subsequently reacts to BiNi.[24] That mechanism differs considerably from the one described in this work.

We have investigated the formation of Bi_2Ir nanoparticles by the polyol process. Synthesis of intermetallic compounds of bismuth and iridium by conventional high-temperature processes is challenging because bismuth evaporates 850 K below the melting point of iridium. We had previously synthesized nanocrystalline Bi_2Ir powder using a microwave-assisted polyol process and thus gained access to the structural and physical properties of this phase.[25] Here, we report our extensive research on the reaction mechanism, which unexpectedly also led to the discovery of a suboxide of Bi_2Ir.

Results and Discussion

The formation of the Bi_2Ir nanoparticles was performed in a microwave assisted polyol process using ethylene glycol (EG). Systematic experiments have been conducted varying temperature, pH value and the metal salts. Products and intermediates were isolated and characterized by powder X-ray diffraction (PXRD), *in-situ* XRD using synchrotron radiation, transmission electron microscopy (TEM), energy-dispersive X-ray spectroscopy (EDX), selected area electron diffraction (SAED), X-ray photoelectron spectroscopy (XPS), UV-Vis spectroscopy, differential scanning calorimetry (DSC), and magnetization measurements.
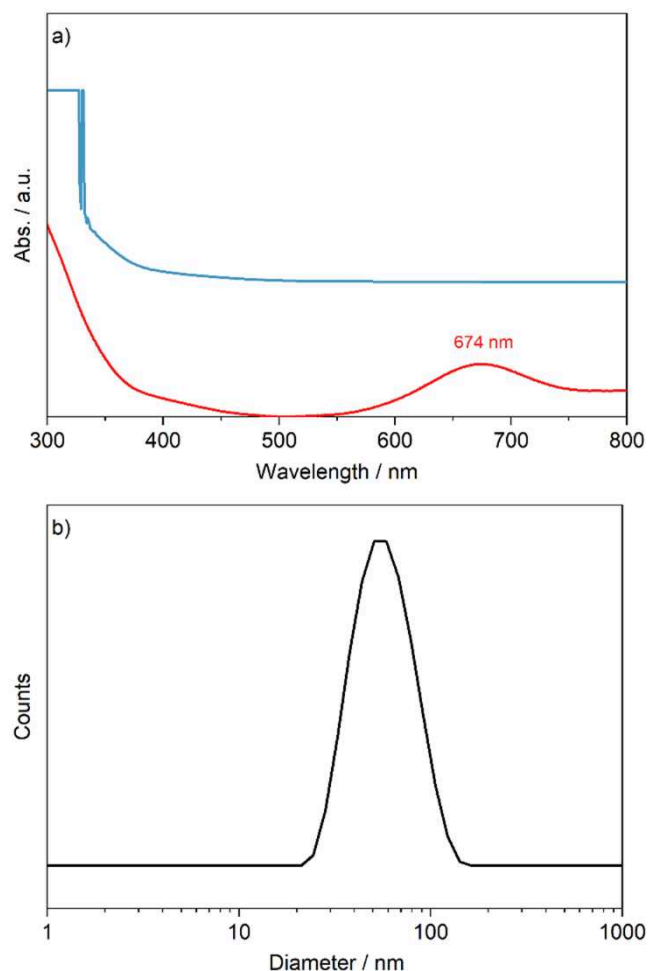
Reduction of Ir(OAc)$_3$ in EG

Since the reduction of bismuth nitrate has already been discussed in our previous work,[24] we focus on the reduction of iridium acetate in this section. Considering the standard potentials of iridium(III) and bismuth(III) in aqueous solutions (Equation 1 and 2), iridium is generally nobler and its cations should therefore be reduced at lower temperature.

$$Bi^{3+} + 3e^- \rightleftharpoons Bi \qquad E° = +0.31\ V \qquad\qquad (1)$$
$$Ir^{3+} + 3e^- \rightleftharpoons Ir \qquad E° = +1.16\ V \qquad\qquad (2)$$
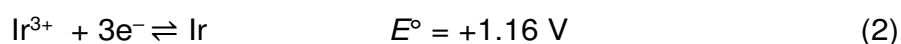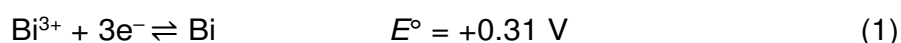
Unlike in water, Ir(OAc)$_3$ dissolves slowly in EG, yielding a green solution that turns deep yellow/brown at concentrations higher than about 3 mol L^{-1}. The acetate anions make the solution basic, which facilitates metal reduction by enhanced deprotonation of EG. Solutions of different concentrations were analyzed by UV-Vis spectrometry (Figure 1a). The UV-Vis spectrum of the green solution (about 10 mmol L^{-1}) showed the expected absorption in the red region at 674 nm and a steeply increasing absorption in the UV region. Interestingly, the absorption spectrum of the higher concentrated, brownish solution showed no absorption bands in the visible region. Instead, dynamic light scattering revealed the presence of particles with an average diameter of 54 nm, which cause the color change due to the Tyndall effect (Figure 1b). This process is partially reversible by adding additional solvent, indicating high reactivity of the freshly formed nanoparticles, which probably consist of elemental iridium; an

isolation and characterization of these particles was not possible. In diluted EG solutions of Ir(OAc)$_3$ (e.g. 10 mmol L^{-1}), the reduction of iridium(III) to the metal occurs only upon heating to about 120 °C. Bismuth(III) from dissolved Bi(NO$_3$)$_3$ is reduced at approx. 215 °C, in accordance with its less positive standard potential.

**Figure 1.** a) UV-Vis spectra of low (red) and high (blue) concentrated Ir(OAc)$_3$ solutions in EG with b) showing the size distribution of particles in highly concentrated solutions.

Co-Reduction of Bi(NO$_3$)$_3$ and Ir(OAc)$_3$ in EG

Upon heating Bi(NO$_3$)$_3$ and Ir(OAc)$_3$ in EG to about 160 °C, a black precipitate was obtained, which was later identified as the new suboxide Bi$_4$Ir$_2$O (see below). The reaction was further traced in a series of experiments in which the reaction temperature was gradually increased (10 min reaction time in each case). The higher the reaction temperature, the more intense and sharper the reflections of the new phase appeared in the X-ray diffractograms (Figure 2). In the powder patterns of the samples that had been reacted at 220 °C or 230 °C, two sharp reflections located at 30.30° and 30.69° became visible at the position of the previously broad one at 2θ = 30.5°. Similarly, the broad reflection at 2θ = 55.64° splits into two reflections at

55.57° and 55.81°. The first evidence of the formation of Bi_2Ir was found in the diffractogram of the 240 °C sample. The pattern of the 250 °C sample, on the other hand, showed the formation of well-crystallized Bi_2Ir and only small traces of the suboxide. Accordingly, there appears to be a fairly well defined range for the existence of the suboxide.
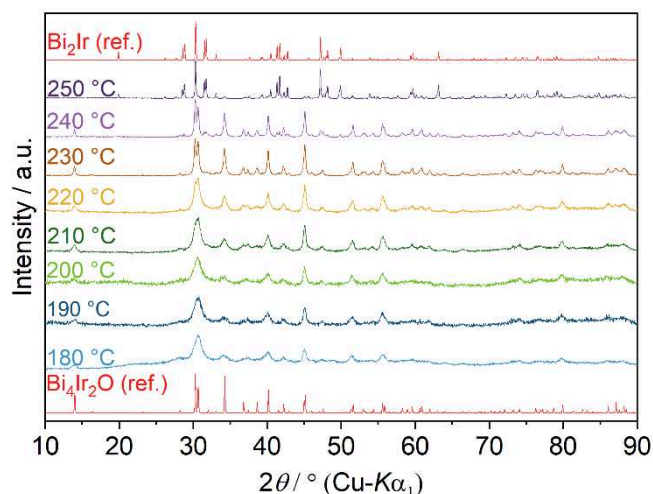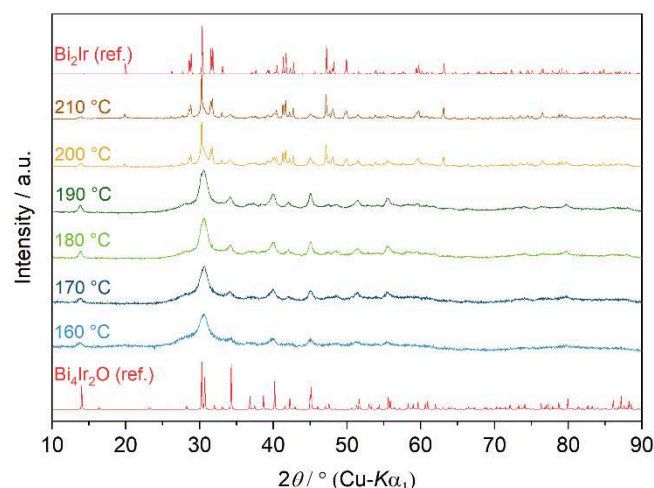

Figure 2. PXRD patterns of solid reaction products obtained from the reaction of $Bi(NO_3)_3$ and $Ir(OAc)_3$ at different temperatures after 10 min reaction time. Bi_2Ir (ref.) and Bi_4Ir_2O (ref.) are calculated diffraction patterns based on the crystal structures of Bi_2Ir (ICSD entry CSD-424397) and Bi_4Ir_2O (see below).

Further information on the size and morphology of the particles formed at the different temperatures was obtained by TEM experiments. At 180 °C, quasi-spherical, well-dispersed particles were observed (Figure 3a), which exhibit a narrow size distribution with diameters of 24 ± 5 nm (Figure S1a). Particles obtained at 220 °C display the same morphology and size distribution (Figure 3b and S1b). The dark contrast in the center of some particles could indicate nuclei of elemental iridium, which has almost twice the density of Bi_4Ir_2O. At 250 °C the Bi_2Ir phase displays strongly agglomerated particles (Figure 3c).
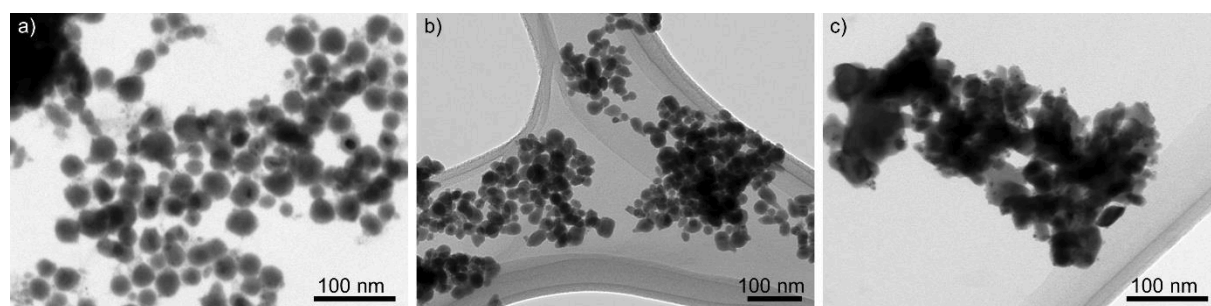
Figure 3. TEM images of precipitates isolated at a) 180 °C (Bi_4Ir_2O) and b) 220 °C (Bi_4Ir_2O) showing quasi-spherical particles with diameters of 24 ± 5 nm and c) 250 °C (Bi_2Ir) displaying strong agglomeration.

Since a higher pH value promotes the reduction of metal ions in the polyol process,[15] the syntheses were repeated with the addition of NaOH. In fact, the PXRD patterns show that the formation of Bi_2Ir already occurs at the much lower temperature of 200 °C (Figure 4). Small residues of the suboxide are still present, as evidenced by the reflection at $2\theta = 13°$ and the shoulder at 30.7°. The formation of Bi_4Ir_2O also starts at lower temperatures than under neutral conditions. Even higher pH values further reduce the phase formation temperature to about 130 °C.


Figure 4. PXRD patterns of solid reaction products obtained from the reaction of $Bi(NO_3)_3$ and $Ir(OAc)_3$ with added NaOH at various temperatures after 10 min reaction time. Bi_2Ir (ref.) and Bi_4Ir_2O (ref.) are calculated diffraction patterns based on the crystal structures of Bi_2Ir (CSD-424397) and Bi_4Ir_2O (see below).

The isolated suboxide can be re-dispersed in EG and the reduction towards Bi_2Ir completes upon heating at temperatures above 240 °C.

In addition to the batch processes, we have carried out *in-situ* XRD measurements at the P23 beamline at DESY Hamburg using synchrotron radiation with a wavelength of 0.61992 Å. To achieve significant scattering intensity, the reaction was performed with the fourfold concentration of the starting materials. As preliminary experiments had shown, the reaction process and reaction products are independent of the concentration except for small temperature changes due to the pH value. In order to achieve a minimal pathway of the synchrotron X-ray beam through the reaction volume, a modified glass reactor containing an inserted glass tube was applied.[26] The reactor holder comprises an integrated stirring and heating system. In addition, it contains two openings for the X-ray beam inlet and outlet.[27] The experiment started with linear heating of the sample from room temperature to about 130 °C; this temperature was reached after 10 min and then kept largely constant for the remaining 20 min. Since temperature but not duration is the primary factor in the reaction process the longer reaction time served only to ensure that a certain product amount was formed to produce sufficient scattering intensity. After about 9 min, reaching 125 °C, the abrupt formation

of Bi_4Ir_2O was observed (Figure 5a). As the reaction progressed, the intensity of the reflections increased, uniformly for all, indicating isotropic particle growth (Figure 5b). An exception is the reflection at $2\theta = 16.06°$, which can be assigned to the (111) plane of elemental iridium. The formation of iridium occurs simultaneously to the suboxide; the reflection intensity decreases with time until it reaches a plateau. We assume that iridium is partially incorporated into the particles of the suboxide after it has acted as a seed for particle growth (see TEM images above).
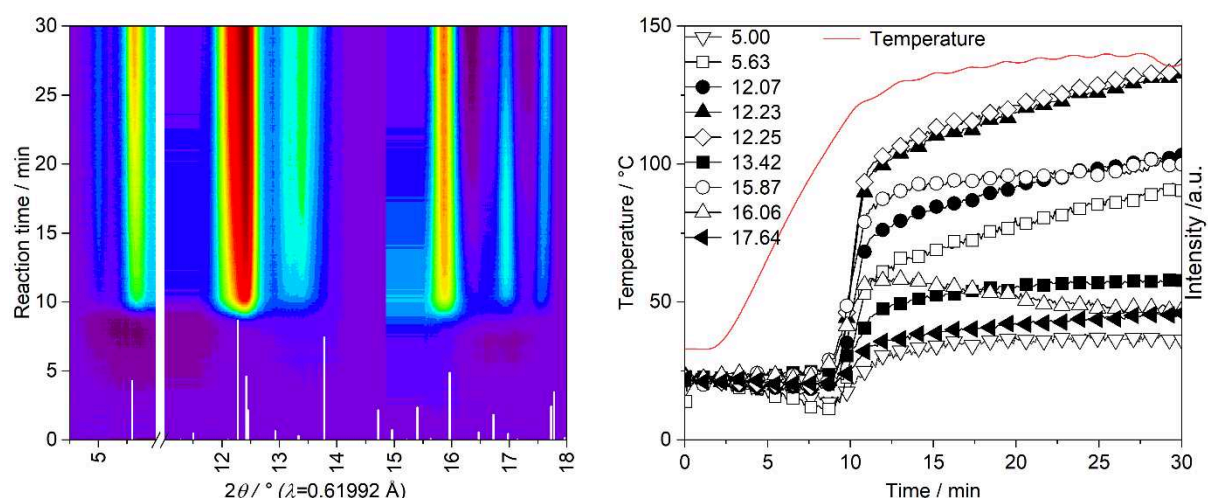

Figure 5 a) *In-situ* XRD measurement monitoring the co-reduction of $Bi(NO_3)_3$ and $Ir(OAc)_3$ in alkaline EG. The interval $6.3° \leq 2\theta \leq 11°$, which shows a strong contribution of diffuse scattering by the glass vessel (Figure S2), was excised. The calculated diffraction pattern of Bi_4Ir_2O is shown as white lines. b) Evolution of temperature and reflection intensities over the duration of the experiment.

In order to trace the oxygen source for the suboxide Bi_4Ir_2O, syntheses were carried out under argon atmosphere with different starting materials (Figure 6). The reaction of $Bi(NO_3)_3$ and $Ir(OAc)_3$ under argon yielded the suboxide, which led to the conclusion, that atmospheric oxygen is not essential for its formation. In a second experiment, $Bi(NO_3)_3$ was substituted by $Bi(OAc)_3$, which resulted in an amorphous powder, if performed under argon. The same reaction in air also yielded a predominantly amorphous powder, although small amounts of Bi_4Ir_2O were also found. In the latter case, $Bi(OAc)_3$ might have reacted with oxygen to $BiO(OAc)$, which could then act as an oxygen donor. Reacting $Bi(NO_3)_3$ with $IrCl_3$ resulted in poorly crystalline $BiOCl$ accompanied by elemental iridium independent of the atmosphere. Using $K_2[IrCl_6]$ as iridium precursor also led to $BiOCl$. Remarkably, $K_2[IrCl_6]$ reacts differently depending on the bismuth salt. $K_2[IrCl_6]$ and $Bi(NO_3)_3$ form a mixture of $BiOCl$ and iridium, while with $Bi(OAc)_3$ an amorphous black powder, probably with the same composition, was obtained. In summary, nitrate seems to be a crucial component for the formation of Bi_4Ir_2O and the likely

source of oxygen. However, traces of water – either from the starting materials or as a product of the condensation of EG at higher temperatures − cannot be excluded as oxygen source. Chloride ions and probably other halide ions, on the other hand, are harmful because they allow the formation of stable bismuth oxide halides.
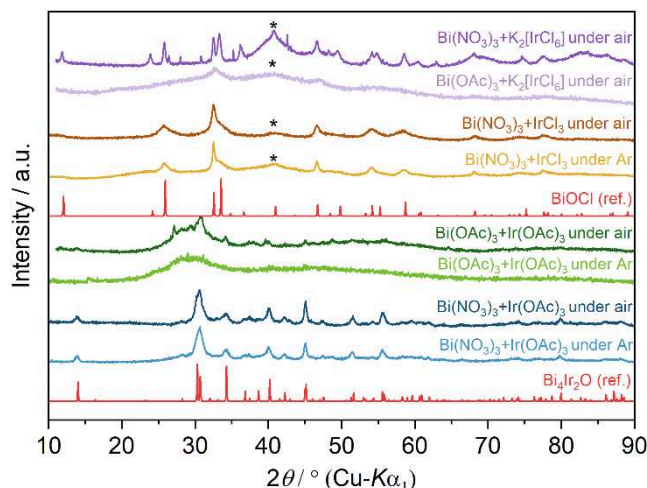

Figure 6. PXRD patterns of solid products from reactions using different starting materials under atmospheric and inert conditions after 15 min reaction time at 160 °C. Bi_2Ir (ref.) and Bi_4Ir_2O (ref.) are calculated diffraction patterns based on the crystal structures of Bi_2Ir (CSD-424397) and Bi_4Ir_2O. The reflections marked with an asterisk are attributed to elemental iridium.

Characterization of Bi_4Ir_2O

A combined elemental analysis by ICP-OES and EDX spectroscopy revealed the composition Bi : Ir : O = 56(1) : 28(1) : 16(1) for the new suboxide, consistent with the molecular formula Bi_4Ir_2O within the given accuracy of the methods. An EDX mapping showed a homogenous distribution of the constituent elements across the particles (Figure S3).

Further evidence for the oxygen content was provided by high-temperature (HT) PXRD measurements of Bi_4Ir_2O in vacuum. The powder patterns show a slow degradation of the primary phase at around 255 °C as can be seen by the decrease in intensity and broadening of the main reflection at approx. $2\theta \approx 30°$. At 255 °C new reflections arise that can be attributed to α-Bi_2O_3 (Figure 7). Furthermore, subtle reflections of elemental iridium are visible, mainly at $2\theta = 40.29°$, which indicates thermal decomposition of Bi_4Ir_2O. Residual reflections can be attributed to the Al_2O_3 sample holder. Following the high temperature studies, PXRD measurements of the respective products were performed at room temperature, to obtain higher quality patterns. These undoubtedly showed Bi_2O_3 and Ir (Figure S4).
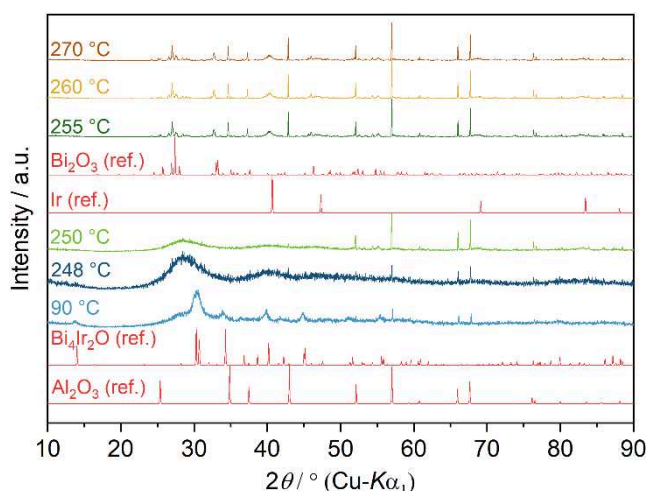
Figure 7. HT-PXRD patterns of a Bi_4Ir_2O sample in the temperature range of 248 °C to 270 °C. Bi_4Ir_2O (ref.), Ir (ref.), Bi_2O_3 (ref.) and Al_2O_3 (ref.) are calculated diffraction patterns based on the crystal structure of Bi_4Ir_2O, Ir (CSD-640730), Bi_2O_3 (CSD-15072), and Al_2O_3 (CSD-160607).

The reaction was also monitored by DSC measurements. Heating curves were taken at a rate of 2 K min^{-1} under constant argon flow to observe phase transitions in Bi_4Ir_2O (Figure 8). The first endothermic peak (a) was registered at 197.3 °C and corresponds probably to the evaporation of residual EG on the surface of the particles. The very broad second peak (b) with onset at about 260 °C and maximum at 269 °C agrees well with the decomposition temperature of Bi_4Ir_2O and the formation of Bi_2O_3 derived from the HT-PXRD experiment, while the smaller peak at 280 °C might be caused by side reactions due to impurities.
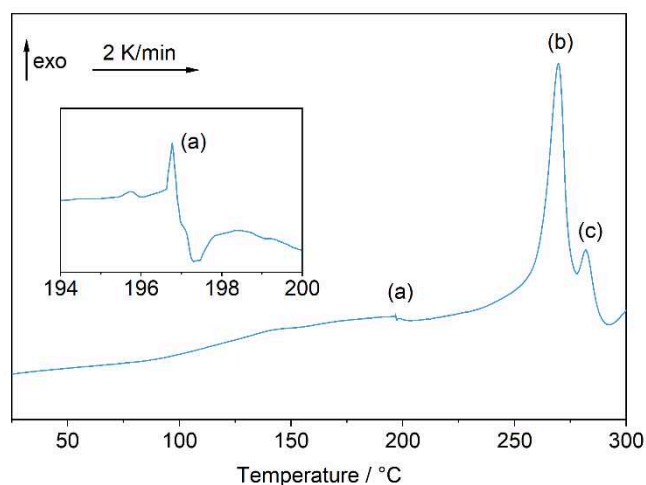
Figure 8. DSC heating curve of a Bi_4Ir_2O sample, showing (a) the evaporation of residual EG, (b) the exothermic decomposition of Bi_4Ir_2O and (c) exothermic peak caused by side reactions due to impurities.

The chemically related suboxide Bi_3IrO_2 has the ability to store and release oxygen after exposure to reducing agents, while largely maintaining its structure.[28] Therefore, experiments

were performed to remove oxygen from Bi_4Ir_2O in a topochemical reaction by exposing the powder to $NaBH_4$ or N_2H_4 solutions at different concentrations at 60 °C for 30 min. The PXRD patterns of the thus treated samples showed no visible change in the position or width of their X-ray reflections compared to Bi_4Ir_2O (Figure S5). We attribute the lack of reactivity of Bi_4Ir_2O at this moderate temperature to its layered structure (see below). Bi_3IrO_2, on the other hand, consists of isolated [Bi_3Ir] rods that leave plenty of room for oxygen diffusion in three dimensions. This is reflected in the physical density, which is 13.72 g cm^{-3} for Bi_4Ir_2O, but only 12.11 g cm^{-3} for Bi_3IrO_2.[28] However, at 120 °C, Bi_4Ir_2O is reduced to Bi_2Ir by a stream of H_2 within 30 min.

To complete the characterization, magnetic measurements were conducted. Bi_4Ir_2O is diamagnetic (Figure S6). Only at very low temperatures is a weak paramagnetic contribution observed, which is attributed to ubiquitous traces of paramagnetic.

Crystal and Electronic Structure of Bi_4Ir_2O

Since single-crystals of sufficient size could not be obtained, powder X-ray diffraction was used to determine the structure of Bi_4Ir_2O. Indexing the powder pattern indicated an orthorhombic unit cell with lattice parameters $a = 5.9826(7)$ Å, $b = 4.0121(5)$ Å, and $c = 12.6253(5)$ Å. SAED measurements confirmed these lattice parameters (Figure S7). Despite the broad reflections (nanoparticles) and enormous absorption effects ($\mu = 305$ mm^{-1}), a reasonable structure solution in the space group *Pnma,* including the heavy atoms, was obtained from the integrated PXRD intensities using the charge-flipping method (Figure 9). In agreement with the results of quantum chemical calculations (see below), the oxygen atoms were placed in one of the tetrahedral voids between the intermetallic layers. With respect to the analytical composition, the oxygen position is only half occupied. A final Rietveld refinement showed satisfactory agreement with the experimental pattern (Figure S8, Tables S1 to S3). A fully ordered structure model with maximized O···O distances (5.25 and 5.98 Å, instead of 3.55 Å in the average structure) can be constructed in an enlarged unit cell with $b' = 2b$ (Figure S9, Table S4). However, there is no experimental evidence for a superstructure with long-range order.
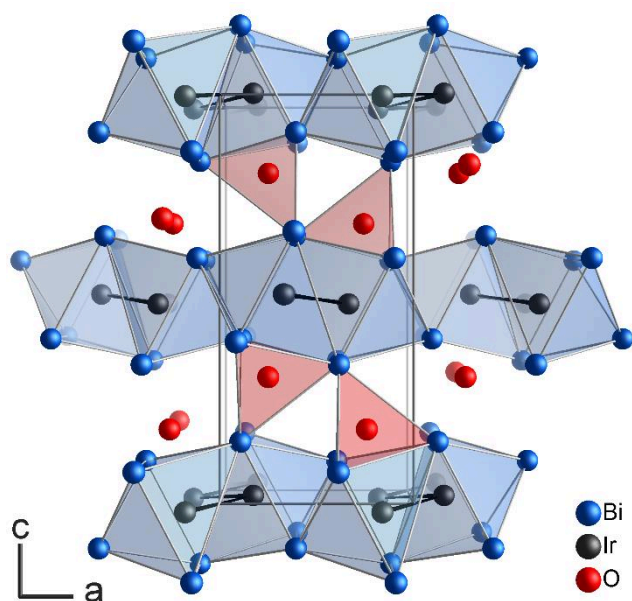
Figure 9. Crystal structure of Bi_4Ir_2O depicting the corrugated layers in the (001) plane with zigzag chains of iridium atoms along the b-axis. One quarter of the tetrahedral voids between the intermetallic layers is occupied by oxygen atoms.

In the crystal structure of Bi_4Ir_2O, each iridium atom is coordinated by six bismuth atoms that form a highly distorted octahedron. The Ir–Bi distances range from 2.70(1) to 2.82(1) Å (average 2.76(1) Å). For comparison, in the arsenopyrite type structure of Bi_2Ir, the range of Ir–Bi distances in the octahedron is 2.68(1) to 2.83(1) Å (average 2.72(1) Å). The $[IrBi_6]$ polyhedra share their edges to form a strongly corrugated layer with the composition Bi_2Ir. The Ir atoms are not equidistant but form zigzag chains parallel to the b-axis with Ir–Ir distances of 2.81(1) Å. The Bi_2Ir layers are stacked along the c-axis. The oxygen atoms in the tetrahedral voids between the intermetallic layers have Bi–O distances of 2.13(2) to 2.52(2) Å. The structure of the suboxide Bi_3IrO_2 can be used for comparison.[28] There, $[Bi_3Ir]$ rods with internal Ir–Ir zigzag chains (2.80 Å) are separated by oxygen atoms. For the tetrahedrally coordinated oxygen atom in Bi_3IrO_2, the Bi–O distances range from 2.26 to 2.92 Å (DFT-based structure optimization).

The stacking sequence in the intermetallic part of Bi_4Ir_2O is $A\gamma B\square C\alpha B\square$, with the Bi atoms forming the packing. This (heavily distorted) double-hexagonal sequence of the suboxide seems to be clearly different from the arsenopyrite-type arrangement in Bi_2Ir, which is represented by $A\gamma_{1/2}B\gamma'_{1/2}$. Nonetheless, the chemical transformation from Bi_4Ir_2O to Bi_2Ir requires mainly the displacement of half of the Ir atoms into adjacent octahedral voids, accompanied by adjustments in the local environment.

To obtain information about the oxidation states in Bi_4Ir_2O, XPS measurements were performed (Figure 10). The 4*f* region of iridium exhibits a pair of peaks that can be fitted by three doublets. Referring to the lower energy part of the doublets, they are located at 60.0 eV (blue), 60.5 eV (green) and 61.4 eV (orange). Compared to elemental iridium (60.9 eV), the peak at 60.0 eV is shifted towards lower binding energies, indicating a reduction.[29] This had also been observed for the suboxide Bi_3IrO_2, where the calculated charge distribution corresponded to iridium in the oxidation state –I ($5d^{10}$ configuration).[28] The peak at 60.5 eV corresponds to iridium in a less reduced state. According to the composition and structure of Bi_4Ir_2O, there must be iridium atoms with and without nearby oxygen atoms. This requirement also points towards an ordered superstructure, like the one established in space group $P2_1/n$ (see below), e.g., as the average structure features only one crystallographic Ir position. An oxygen atom withdraws electron density from the bismuth atoms, which is otherwise donated to the iridium atom. As expected, the peaks representing the more (60.0 eV) and the less (60.5 eV) reduced iridium atoms are of similar size. The weaker signal at 61.4 eV represents iridium in a positive oxidation state, probably iridium(IV), which forms readily under alkaline conditions and should be present in EG complexes on the particle surface.

The 4*f* region of bismuth displays four oxidation states. The peaks at 156.9 eV (blue) and 157.3 eV (green) represent bismuth atoms in oxidation states close to elemental bismuth (157 eV), although minor oxidation is indicated. This is expected for an intermetallic layer Bi_2Ir in which bismuth is the electron donor. The peak at 158.5 eV corresponds to an intermediate oxidation state if Bi_2O_3 (159.2 eV) is taken as a reference.[29] These should be bismuth atoms bonded to one or two oxygen atoms. The peak at 159.2 eV indicates complexed bismuth(III) at the surface. In analogy to the related suboxide Bi_3IrO_2, an amorphous shell with a thickness of about 2–4 nm around the nanoparticles can been observed in HR-TEM studies, most likely containing the iridium(IV) and bismuth(III) cations mentioned above (Figure S10).
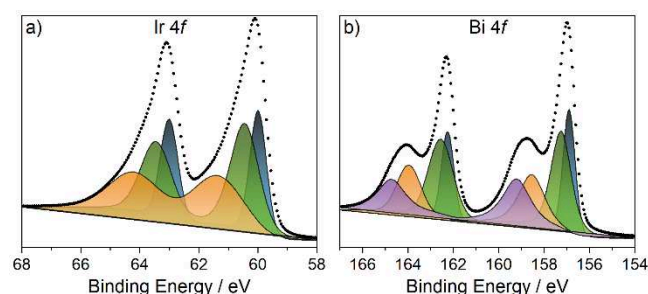
Figure 10. XPS spectra for the 4f regions of iridium (a) and bismuth (b). Dotted lines depict the total spectra. Colored areas represent the contributions of the different species after deconvolution of the total spectrum.

To support the structure solution but also to gain insight into the electronic structure of Bi_4Ir_2O, density functional theory (DFT)-based calculations were performed. Given the experimental uncertainty regarding the oxygen positions, a structure optimization without point symmetry constraints was performed. However, due to the high computational cost for such a heavy-atom structure and lack of experimental evidence for a long-range superstructure in a larger unit cell, we used the experimental unit cell for the suboxide but with full occupancy of the oxygen position, i.e., we performed the calculation for a hypothetical compound "$Bi_4Ir_2O_2$". The resulting structure model (Table S1) is in good agreement with the diffraction data (including space group symmetry) and chemically sound, except for the overpopulated oxygen positions. The density of states (DOS) for "$Bi_4Ir_2O_2$" indicates a metal with a pseudogap 0.8 eV above the Fermi level. Adding two electrons per formula unit in a rigid band model, which corresponds to the reduction to the actual composition Bi_4Ir_2O, shifts the Fermi level exactly into the pseudogap. We have therefore performed an additional full-relativistic DFT calculation for the correct composition Bi_4Ir_2O in the above mentioned, hypothetical, ordered superstructure with maximized O⋯O distances ($b' = 2b$, space group $P\,1\,1\,2_1/n$). As expected, the Fermi level lies in the pseudogap, which has a DOS minimum of about eight states per formula unit (Figure 11).
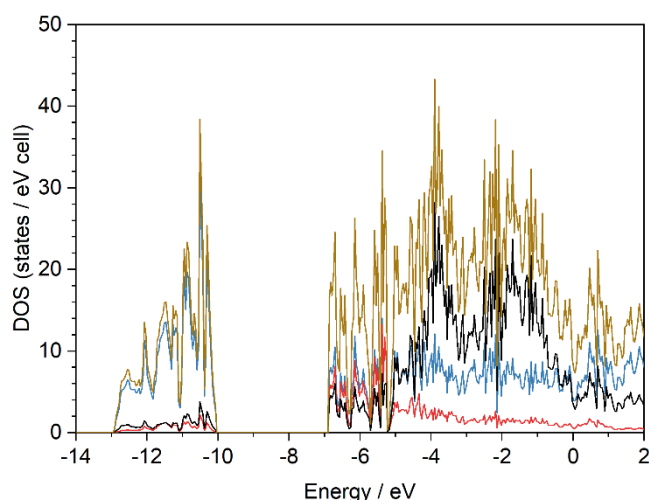
Figure 11. Density of states calculated for Bi_4Ir_2O in a hypothetical oxygen-ordered superstructure. Gold: total density of states, blue: Bi contribution, black: Ir contribution, red: O contribution

The DOS and the band structure (Figure 12) show that the states around the Fermi level are dominated by the two metals. The oxygen content is mainly determining the position of the Fermi level. Consequently, the band dispersion around the Fermi level reflects the layered character of the intermetallic part of the Bi_4Ir_2O structure. Along the stacking direction, the bands are flat and there is even a gap of about 0.2 eV above the Fermi level. In all directions

that are parallel to the layers, covalent bonding between the metal atoms causes substantial dispersion of the bands. Bi_4Ir_2O can thus be regarded as a pseudo two-dimensional metal.
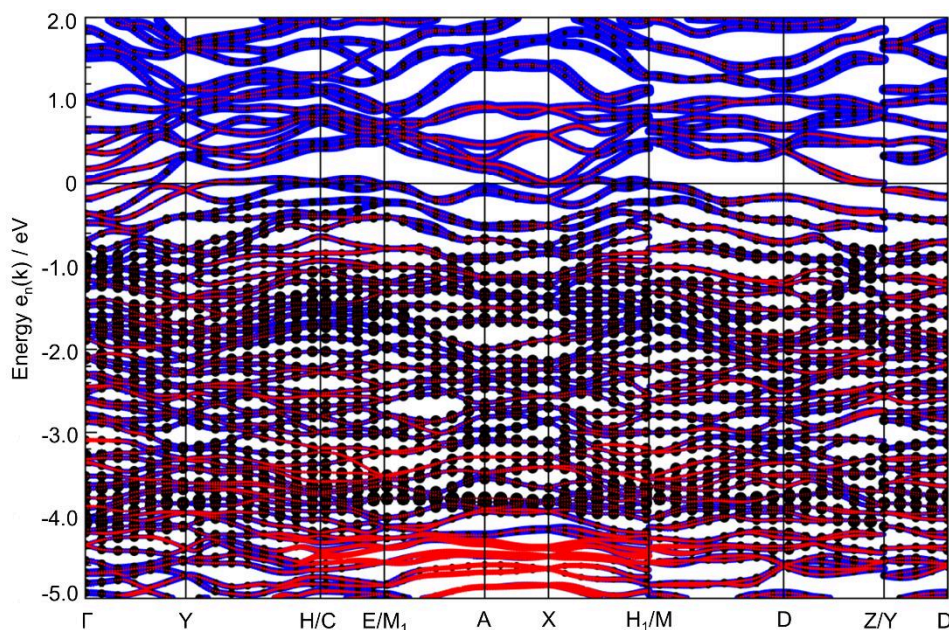
Figure 12. Electronic band structure of Bi_4Ir_2O calculated for a hypothetical oxygen-ordered superstructure. The dot sizes mark the weights of the elements to the bands. Blue: Bi, black: Ir, red: O. In order to reveal the mutual contribution of the two metals at the Fermi level, the Ir contribution is shown with a reduced number of points.

Conclusion

The systematic investigation of Bi_2Ir nanoparticle formation in the (microwave-assisted) polyol process revealed a two-stage scenario that is temperature controlled. First, the starting materials are partially reduced to the new intermetallic suboxide Bi_4Ir_2O, where iridium nuclei may act as a nucleation site for particle growth. In a second step, at higher temperature, the intermediate phase is fully reduced to the Bi_2Ir phase. As had been observed in many other cases, an alkaline medium lowers the reaction temperature for the reduction of the metal cations by deprotonation of the polyol. This is the case for the formation of Bi_4Ir_2O as well as Bi_2Ir. The formation of Bi_4Ir_2O depends on the starting materials, with $Bi(NO_3)_3$ and $Ir(OAc)_3$ being the only pair tested that produces the suboxide. Chloride ions prevent the formation of the suboxide as they lead to the precipitation of BiOCl. The crystal structure of Bi_4Ir_2O consists of intermetallic layers that are separated by oxide ions. Upon heating under reducing conditions, Bi_4Ir_2O can be converted to Bi_2Ir, while otherwise it decomposes to Bi_2O_3 and elemental Ir.

Experimental Section

Chemicals

Ethylene glycol (Fluka 99.5 %) was used as purchased. The following iridium(III) and bismuth(III) salts were used: $Bi(NO_3)_3 \cdot 5H_2O$ (VWR, 98 %), $Bi(OAc)_3$ (abcr, 99%) stored under argon), $Ir(OAc)_3$ (Chempur, 99 %), $IrCl_3$ (abcr, 48% Ir), $K_2[IrCl_6]$ (Sigma Aldrich, technical grade). For some experiments, a 1 M solution of NaOH (Grüssing, 99 %) in EG was used. Reduction experiments were performed with $NaBH_4$ (Aldrich, 99 %) and N_2H_4 (Merck, 80 vol.-% in aqueous solution).

Synthesis

All laboratory synthesis experiments were performed in a microwave-assisted polyol process in an Anton Paar Monowave 400 synthesis microwave, using 30 mL vessels equipped with magnetic stirring bars that ensured proper mixing of the reagents. For each synthesis the respective bismuth (0.1 mmol) and iridium (0.05 mmol) compounds were mixed with 10 mL of EG. In case of addition of 1 M NaOH solution, 2 mL were added to 8 mL of EG. After dissolution of the starting materials, the reaction mixtures were heated by microwave radiation to the desired temperature within 2 min. At the end of the reaction time, the sample was cooled to 60 °C inside the microwave device by a stream of air and then removed. The precipitates were isolated by centrifugation at 4400 rpm, washed three times with ethanol to remove residual solvent, and dried overnight under vacuum at room temperature.

In case of the synchrotron experiments, 0.4 mmol of $Bi(NO_3)_3$ and 0.2 mmol of $Ir(OAc)_3$ with addition of 2 mmol of NaOH (2 mL of 1 M NaOH solution) were dissolved in 8 mL of EG. Afterwards, the solution was heated in a glass vessel to 130 °C under mild stirring.

Syntheses under inert conditions were performed in a 25 mL two-neck round-bottom flask. First EG was heated to 120 °C in an oil bath to evaporate residual water. The flask was then closed and EG degassed with argon at 50 °C under mild stirring in order to eliminate oxygen from the system. When the temperature reached 60 °C the salts were added through a funnel. The system has been degassed for additional 15 min, before the temperature of the oil bath was set to 165 °C for 10 min. After the solution has cooled down, the precipitates were collected and immediately measured without washing to reduce oxygen exposure time.

Reduction experiments were carried out with a freshly prepared powder of Bi_4Ir_2O, which was dispersed in water in a 25 mL flask and treated by ultra-sonication for 5 min. A 1 M solution of

NaBH$_4$ was prepared in water and added to the suspension in molar ratios of 10:1, 20:1 and 50:1 relative to Bi$_4$Ir$_2$O. Alternatively, hydrazine solution was added in the same molar ratios. The reaction mixtures were then heated to 60 °C in an oil bath for 30 minutes. The powder was isolated by centrifugation and measured immediately without further washing.

Characterization

PXRD patterns were recorded at 296(1) K with an X'Pert Pro MPD diffractometer (PANalytical) or Empyrean (PANalytical) equipped with a Johansson monochromator using Cu-Kα_1 radiation (λ = 1.54056 Å) and a Pixcel-1D detector in Bragg-Brentano setup. HT-XRD experiments were performed on a Empyrean (PANalytical) powder X-ray diffractometer using Cu-Kα_1 radiation (λ = 1.54056 Å) and Pixcel-3D Detector in 1D scanning mode (255 active channels). An Anton-Paar HTK 1200N furnace was used to reach the desired temperatures with the sample held under vacuum. An automatic sample height correction was used to compensate the thermal expansion of the holder. After heating with 5 K s^{-1} to the desired temperature and a subsequent waiting time of 5 min, the sample was measured with a scan time of 80 min.

Synchrotron experiments were performed at the DESY Hamburg P23 beamline, using X-rays with a wavelength of 0.61992 Å. Powder diffraction patterns were recorded every 5 s. A 2D–detector (Teledyne DALSA Rad-icon 2329, Canada) was applied.

UV-vis spectroscopy was performed in double beam mode on a UV-1650PC (Shimadzu) in standard quartz glass cuvettes.

XPS spectra were recorded on a PHI 5600 spectrometer (Perkin Elmer) utilizing Mg-$K\alpha_1$ and monochromated Al-$K_{\alpha 1}$ radiation. The values are referenced to the standard C1s binding energy of 284.8 eV.

DSC data was obtained under argon with a DSC1 (Mettler Toledo) using an empty aluminum crucible as reference.

For TEM investigations, a Tecnai G2 (FEI) with an acceleration voltage of 200 kV and a LaB$_6$ cathode was used. The diameter of the particles was obtained with the ImageJ software (Build 1.53e).[30] Images were imported and the diameters measured manually to avoid false identification of particles by the software. EDX and SAED measurements were performed on a JEM-F200 (JEOL) with an acceleration voltage of 200 kV produced by a cold field emission gun.

Structure Determination of Bi$_4$Ir$_2$O

The material was prepared onto a sample holder with a cavity of 16 mm diameter. The powder pattern was recorded in a 2θ range from 10 to 90° with a step size of 0.026° using the

equipment described above. To increase the count rate at higher angles, a variable divergence slit was used. The illuminated sample area was kept constant at 12mm (axial) × 8 mm (equatorial). For indexing, Le Bail refinement and Rietveld refinement the program *TOPAS Academic* was used, while structure solution was carried out with *JANA2006* and the charge-flipping method of the program *SUPERFLIP* implemented in the *JANA2006* software.[31–34] The peak profiles were modeled with the fundamental parameter approach implemented in *TOPAS*. The background was modeled with Chebychev polynomials of 20th order. The reflections of Bi_4Ir_2O were indexed by iterative use of singular value decomposition, leading to a primitive orthorhombic unit cell with a volume of about 303 Å[3].[35] Lattice and peak profile parameters were refined by the Le Bail method and subsequently fixed for the structure refinement.[36] For the Rietveld refinement (Figure S8), profile, lattice, and structural parameters were released iteratively. The positions and isotropic displacement factors of the Bi and Ir atoms were refined freely. Oxygen atoms were placed in the octahedral and tetrahedral voids between the intermetallic layers, and their occupancies were refined to identify the most probable position, which turned out to be one of the tetrahedral voids. DFT-based geometry optimization of this model yielded Bi–O distances that were retained for final refinement of the structure model. The obtained crystallographic parameters and agreement factors are listed in Table S1. Graphics of the crystal structures were created with Diamond.[37]

Computational Details

Solid state calculations were performed with the FHI-aims program[38] and the FPLO package[39] at gradient-corrected density functional theory level using the PBE functional[40]. Structure optimization for the "hypothetical" fully oxygen occupied compound with chemical formula $Bi_4Ir_2O_2$ was carried out in P1 symmetry with the FHI-aims program at scalar relativistic level employing a k-grid with 8*12*4 points.

Final band structure calculations for the supercell of a hypothetically ordered superstructure (doubled along the b-axis) of the compound Bi_4Ir_2O were performed with the FPLO program at full relativistic level using a k-grid of 8*6*4 points. Band structure analysis including individual atomic weights and partial density of states have equally been carried out with the FPLO utility packages.

References

1   F. Fievet, J. P. Lagier, B. Blin, B. Beaudoin and M. Figlarz, *Solid State Ion.*, 1989, **32–33**, 198–205.

2   H. Dong, Y. C. Chen and C. Feldmann, *Green Chem.*, 2015, **17**, 4107–4132.

3   T. S. Rodrigues, M. Zhao, T. H. Yang, K. D. Gilroy, A. G. M. da Silva, P. H. C. Camargo and Y. Xia, *Chem. - A Eur. J.*, 2018, **24**, 16944–16963.

4   F. Bonet, C. Guéry, D. Guyomard, R. Herrera Urbina, K. Tekaia-Elhsissen and J. M. Tarascon, *Solid State Ion.*, 1999, **126**, 337–348.

5   J. Teichert, M. Heise, J. H. Chang and M. Ruck, *Eur. J. Inorg. Chem.*, 2017, **2017**, 4930–4938.

6   S. Bundli, P. Dhak, M. Jensen, A. E. Gunnæs, P. D. Nguyen, H. Fjellvåg and A. O. Sjåstad, *J. Alloys Compd.*, 2019, **779**, 879–885.

7   B. M. Leonard, N. S. P. Bhuvanesh and R. E. Schaak, *J. Am. Chem. Soc.*, 2005, **127**, 7326–7327.

8   A. Salati, A. Ramazani and M. Almasi Kashi, *J. Magn. Magn. Mater.*, 2020, **498**, 166172.

9   T. Matsumoto, K. Takahashi, K. Kitagishi, K. Shinoda, J. L. Cuya Huaman, J. Y. Piquemal and B. Jeyadevan, *New J. Chem.*, 2015, **39**, 5008–5018.

10   K. Takahashi, S. Yokoyama, T. Matsumoto, J. L. C. Huaman, H. Kaneko, J.-Y. Piquemal, H. Miyamura and J. Balachandran, *New J. Chem.*, 2016, **40**, 8632–8642.

11   K. Mrad, N. Khemiri, F. Schoenstein, S. Mercone, M. Ben Messaouda, M. Abderrabba and S. Messaoudi, *J. Chem. Sci.*, 2019, **131**, 1–7.

12   S. Okumoto and Y. Kitagawa, *Chem. Lett.*, 2021, **50**, 672–675.

13   J. Teichert, T. Doert and M. Ruck, *Dalt. Trans.*, 2018, **47**, 14085–14093.

14   H. Kaneko, T. Matsumoto, J. L. Cuya Huaman, M. Ishijima, K. Suzuki, H. Miyamura and J. Balachandran, *Inorg. Chem.*, 2021, **60**, 3025–3036.

15   K. J. Carroll, J. U. Reveles, M. D. Shultz, S. N. Khanna and E. E. Carpenter, *J. Phys. Chem. C*, 2011, **115**, 2656–2664.

16   B. M. Leonard and R. E. Schaak, *J. Am. Chem. Soc.*, 2006, **128**, 11475–11482.

17   R. E. Cable and R. E. Schaak, *Chem. Mater.*, 2005, **17**, 6835–6841.

18   N. L. Henderson and R. E. Schaak, *Chem. Mater.*, 2008, **20**, 3212–3217.

19   P. Canaud, R. Mahayri, F. Schoenstein, E. Gautron, K. L. Tan, T. Chauveau, J. M. Morelle, F. Maroteaux and N. Jouini, *J. Electron. Mater.*, 2019, **48**, 4637–4646.

20   K. Takahashi, S. Yokoyama, T. Matsumoto, J. L. Cuya Huaman, H. Kaneko, J. Y. Piquemal, H. Miyamura and J. Balachandran, *New J. Chem.*, 2016, **40**, 8632–8642.

21   A. J. Biacchi and R. E. Schaak, *ACS Nano*, 2011, **5**, 8089–8099.

22   J. Teichert and M. Ruck, *Eur. J. Inorg. Chem.*, 2019, **17**, 2267–2276.

23   K. Mrad, F. Schoenstein, H. T. T. Nong, E. Anagnostopoulou, A. Viola, L. Mouton, S. Mercone, C. Ricolleau, N. Jouini, M. Abderraba, L. M. Lacroix, G. Viau and J. Y. Piquemal, *CrystEngComm*, 2017, **19**, 3476–3484.

24   M. Smuda, C. Damm, M. Ruck and T. Doert, *ChemistryOpen*, 2020, **9**, 1085–1094.

25   R. Boldt, A. Grigas, M. Heise, T. Herrmannsdörfer, A. Isaeva, S. Kaskel, D. Köhler, M. Ruck, R. Skrotzki and J. Wosnitza, *Z. Anorg. Allg. Chem.*, 2012, **638**, 2035–2043.

26   N. Pienack, L. R. Arana, W. Bensch and H. Terraschke, *Crystals*, 2016, **6**, 157(1–14).

27   P. Polzin, I. V. Eliani, J. Ströh, M. Braun, N. Ruser, N. Heidenreich, P. Rönfeldt, F. Bertram, C. Näther, S. Wöhlbrandt, M. Suta and H. Terraschke, *Phys. Chem. Chem. Phys.*, 2018, **20**, 7428–7437.

28   M. Heise, B. Rasche, A. Isaeva, A. I. Baranov, M. Ruck, K. Schäfer, R. Pöttgen, J. P. Eufinger and J. Janek, *Angew. Chemie - Int. Ed.*, 2014, **53**, 7344–7348.

29   J. F. Moulder, W. F. Stickle, P. E. Sobol and K. D. Bomben, *Handbook of X-ray photoelectron spectroscopy: a reference book of standard spectra for identification and interpretation of XPS data*, Perkin-Elmer Corporation, Eden Prairie, USA, 1992.

30   C. A. Schneider, W. S. Rasband and K. W. Eliceiri, *Nature Methods*, 2012, **9**, 671–675.

31   A. A. Coelho, J. Evans, I. Evans, A. Kern and S. Parsons, *Powder Diffr.*, 2011, **26**, S22–S25.

32   A. A. Coelho, *J. Appl. Crystallogr.*, 2018, **51**, 210–218.

33   L. Palatinus and G. Chapuis, *J. Appl. Crystallogr.*, 2007, **40**, 786–790.

34   V. Petrícek, M. Dušek and L. Palatinus, *Z. Kristallogr. - Cryst. Mater.*, 2014, **229**, 345–352.

35   A. A. Coelho, *J. Appl. Crystallogr.*, 2003, **36**, 86–95.

36   A. Le Bail, H. Duroy and J. L. Fourquet, *Mater. Res. Bull.*, 1988, **23**, 447–452.

37   K. Brandenburg, *Diamond 4: Crystal and Molecular Structure Visualization*, Crystal Impact GbR, Bonn, Germany, 2017.

38   V. Blum, R. Gehrke, F. Hanke, P. Havu, V. Havu, X. Ren, K. Reuter and M. Scheffler, *Comput. Phys. Commun.*, 2009, **180**, 2175–2196.

39 H. Eschrig, *Phys. Rev. B: Condens. Matter Mater. Phys.*, 1999, **59**, 1743–1757.

40 J. P. Perdew, K. Burke and M. Ernzerhof, *Phys. Rev. Lett.*, 1996, **77**, 3865–3868.